Wavelength-dependent variations of the electron characteristics in laser-induced plasmas: a combined hydrodynamic and adiabatic expansion modelling and time-gated, optical emission imaging study

Hao Liu* and Michael N.R. Ashfold,

School of Chemistry, University of Bristol, Bristol, U.K., BS8 1TS

and

David N. Meehan and Erik Wagenaars,

York Plasma Institute, Department of Physics, University of York, York, U.K., YO10 5DD

Present address:

College of Advanced Interdisciplinary Studies, National University of Defence Technology, Changsha 410073, Hunan, P.R. China

Corresponding authors:

mike.ashfold@bristol.ac.uk

erik.wagenaars@york.ac.uk

Abstract

The spatial and temporal evolution of the absolute electron densities and temperatures in plasmas formed by nanosecond pulsed laser ablation of silicon in vacuum at two wavelengths (1064 and 532 nm), at similar irradiances, have been explored by complementary simulation (using combined hydrodynamic and adiabatic models) and experiment. Modelling the laser-target and laser-plume interactions with the POLLUX code reveals the evolving composition and dynamics of the laser induced plasma (LIP) during the incident laser pulse: 532 nm irradiation causes more ablation, but the LIP formed by 1064 nm excitation has a higher average charge state and expands faster. The experimental data, from analysis of Stark broadened line shapes of Si^{III} and Si^{IV} cations in time-gated, position- and wavelength-resolved images of the plume emission, allow characterisation of the plume dynamics at later times. These dynamics are compared with predictions from two forms of adiabatic expansion model. Both take as input parameters the plume properties returned by the POLLUX simulations for the end of the laser pulse, but differ according to whether the initial plasma is assumed isothermal or isentropic. The study illustrates: the important λ-dependences of the target absorption coefficient (in establishing the ablated material density) and of electron–ion inverse bremsstrahlung absorption (in coupling laser radiation into the emergent plasma); the extents to which these interactions, the relative ablation yields and the plume expansion dynamics depend on λ; and the importance of identifying appropriate initial conditions for adiabatic expansion modelling of LIP in vacuum.

I INTRODUCTION

Pulsed laser ablation (PLA) is often viewed as a mature technology, with applications in many areas of science and engineering. PLA encompasses many levels of complexity, however, and questions remain regarding many of the fundamentals. The ablation process itself involves a time evolving amalgam of photon – (target) electron interactions, energy transfer from the electrons to the lattice, electron emission from the target (both photoemission and thermionic), heavy particle ejection and evaporation from the target, acceleration of charged particles released from the target surface and laser interactions, ionization, recombination, *etc.*, within the plume of ejected material. The efficiency of the laser-plume interactions determines the extent to which the target surface is shielded from the later part of the incident laser pulse. Many prior investigations of laser induced plasmas (LIPs) have sought to investigate the sensitivity of their characteristics (*e.g.* the electron and/or ion densities, plasma temperature, expansion velocity, *etc.*) to experimental parameters like the incident laser irradiance, ϕ,[1] pulse duration, δt,[2,3] spot size on the target (radius, R),[4] wavelength, λ,[5-13] and the identity and pressure (p) of any background gas.[14]

Here we report complementary experimental and modelling studies of LIPs produced by PLA of a Si target in vacuum using nanosecond (ns) laser pulses of different wavelength (λ = 1064 and 532 nm), while maintaining ϕ, δt and R constant. The experimental component employs time-gated optical emission spectroscopy (OES) imaging methods to determine temporally and spatially resolved electron densities (N_e) and temperatures (T_e) from Stark broadened spectral line shapes measured during the plume expansion phase of PLA. The line shape analysis does not require local thermodynamic equilibrium (LTE) – an assumption that will rarely be applicable to LIPs produced in vacuum.[15,16] Analyses of the plume accompanying PLA of Si in vacuum have been reported previously,[17] but only at a much shorter wavelength (193 nm) and lower fluences (F < 10 J cm^{-2}). The present experimental data are compared with model outputs for the corresponding ablation in vacuum using a combination of numerical (during the laser pulse) and analytical (after the laser pulse) approaches. A two-dimensional (2-D) Eulerian radiative hydrodynamic simulation code POLLUX [18-20] is used to estimate the evolution of plume properties like size, energy, mass, *etc.* during the laser pulse. The estimations of this hydrodynamic modelling are then used as input parameters for subsequent modelling of the adiabatic expansion into vacuum. The latter modelling employs a self-similar gas dynamics model and two limiting sets of initial conditions wherein the plasma is assumed to be either spatially isothermal [21] or isentropic.[22] Using the POLLUX outputs as inputs removes the need for any fitting (or use of experimental data) to determine the initial conditions for the oft-used adiabatic model,[23,24] thereby allowing an unbiased comparison between model and experiment.

Comparative studies that seek to isolate the effect of just one parameter – here wavelength – are relatively rare. Some such studies have been conducted at ambient pressure,[5,11] recognising the interest

in laser induced breakdown spectroscopy (LIBS) for elemental sampling.[25] Here we focus on previous wavelength dependent PLA studies in vacuum employing ns laser pulses. Harilal *et al*.[11] reported a combined modelling (using the HEIGHTS package [26]) and experimental study of the evolving densities and temperatures in LIPs formed by PLA of a tin target in vacuum using CO_2 (λ = 10.6 μm) and Nd:YAG (λ = 1064 nm) laser wavelengths. Optical interferometry provided a measure of the plasma density at early times, while analysis of Stark broadened line shapes in time- and spatially-resolved images of the accompanying emission yielded insight into the evolving electron densities at later times (after cessation of the laser pulse). Interpretation of the experimental data was complicated by the obvious differences in irradiance (which was an order of magnitude higher at λ = 1064 nm) and pulse duration (~5-times longer at λ = 10.6 μm), but did not prevent identification of λ-dependent effects: 1064 nm PLA in this case yielded higher initial plasma densities and higher electron densities, but a lower plume expansion velocity. The present work has closer parallels with recent ns PLA studies of carbon in vacuum at three different excitation wavelengths (λ = 355, 532 and 1064 nm).[12,27] Again, the observed trends were deduced to reflect the wavelength dependences of both the laser-target and laser-plume interactions. 1064 nm PLA yielded the higher plasma temperature (reflecting the much higher plasma absorption coefficient at the longer excitation wavelength), but 355 nm excitation yielded the higher mass and electron densities (reflecting the increased target ablation rate at the shorter wavelength). Being denser, and cooler, the LIP formed at 355 nm also exhibited a lower expansion velocity.[28]

Following a short Experimental and Modelling section, the remainder of this paper is ordered in a way that traces the evolution of the LIP, with the POLLUX simulations of the early time behaviour preceding the experimental measurements and spectral analysis, the results of which are then compared with the adiabatic expansion model outputs. The present data reiterate the importance of the target absorption coefficient on the ablation yield, of electron-ion inverse bremsstrahlung (IB) absorption for coupling laser energy into the ablation plume, and of the balance between these two factors in determining the λ-dependence of the degree of ionization, the electron density and temperature and the plume expansion velocity. They also allow comments on the appropriateness (or otherwise) of different limiting assumptions used in simple adiabatic models of the later plume expansion. An adiabatic model that assumes an isothermal starting distribution is shown to replicate the experimentally observed spatial and temporal evolution of the electron density better than a model assuming an isentropic distribution. However, the agreement with the experimental data is only moderate, and differences between experiment and the theoretical predictions serve to illustrate the importance of defining appropriate initial conditions for these adiabatic models. In particular, numerical modelling shows that under the prevailing experimental conditions neither the isothermal nor isentropic initial spatial profiles are appropriate.

II EXPERIMENTAL AND MODELLING

The apparatus and procedures for the OES experiments have been detailed previously [15,16] and are here summarized only briefly. The fundamental or second harmonic output of a pulsed Nd:YAG laser was incident in the *xz* plane at $\theta = 45°$ to the surface normal (z) and focussed onto the surface of a Si target mounted in vacuum ($p \approx 10^{-7}$ mbar). The size of the irradiated (elliptical) spot on the target surface in both cases was $\approx 4.8 \times 10^{-4}$ cm^2, and the respective pulse energies and full width half maximum (FWHM) pulse durations were ≈68 mJ and $\delta t \approx 7.2$ ns at 532 nm, and ≈79 mJ and $\delta t \approx 8.0$ ns at 1064 nm. These values equate to pulse-averaged irradiances ≈20 GW cm^{-2}. Optical emission from the LIP was imaged using a time-gated intensified charge coupled device (iCCD) coupled to an imaging spectrometer equipped with a photomacrographic objective lens. The entrance slit of the spectrometer was aligned parallel to the target surface normal (*i.e.* in the *xz* plane) and the viewing field (estimated depth < 5 mm) centred on the plume propagation axis. To allow temporal consistency with the modelling, time zero for the experimental studies was defined as the (assumed) start of the laser pulse, with the peak intensity occurring at $t = 8$ ns. Images were collected using short (10 ns) intensifier time gates set to span the period ($t \pm 5$) ns for delays in the range $60 \leq t \leq 120$ ns.

OES measurements within the laser pulse duration are challenging. The early-time evolution of the LIPs of interest was thus investigated using a two-dimensional (2-D) Eulerian radiative hydrodynamic code, POLLUX.[18-20] This code, which has been used in previous simulations of the interaction of laser radiation with a solid target and the subsequent expansion of a LIP,[29-31] solves the three first-order quasi-linear partial differential equations of hydrodynamic flow. The POLLUX calculations assume cylindrical symmetry, with the target and the region above the surface represented by a 2-D (z, r) mesh, where z and r define, respectively, an axis along the target surface normal and the radial coordinate orthogonal to z (with $r = 0$ set at the centre of the laser spot on the target). Thus the model and experimental geometries are not the same (the laser pulses are incident at, respectively, $\theta = 0°$ and 45° to the surface normal). This difference is not expected to have any substantial impact on the comparisons offered later in the article for the following reasons. The plume emission was viewed along an axis perpendicular to the target surface and no evidence for asymmetric plumes or flip-over effects was observed. The laser intensity used in the modelling matches the value deduced with due recognition of the elliptical focal spot that prevailed in the experiment. The critical plasma density (n_c) in the experiments and in the modelling will also differ by a factor of 2 (since $n_{c\theta} = n_c \cos^2\theta$). In practice, this means that the critical density in the modelling will be reached ~10 μm deeper into the plasma – a minor effect for plumes of dimension ~0.5-0.6 mm. Overall, we estimate that any errors in density and temperature due to the difference in incident angle are at most 10%.

Laser-target (leading to melting and vaporisation) and laser-plume (resulting in plasma heating via IB) interactions are both included in POLLUX. The target phase is described by two means; nuclear and thermodynamic terms are handled by tabulated versions of the CHART-D equation of state,[32] while electronic terms, including ionisation within the plume, are determined using the Thomas–Fermi model.[30] Electron and ion temperatures and plasma conductivity are described by a Spitzer-Harm model.[33] Energy and mass transport are treated separately within the code. Mass transport is handled by the Flux Corrected Transport (FCT) model of Boris and Book,[34] while energy transport is modelled using the Incomplete Cholesky-Conjugate Gradient (ICCG) method.[35]

The FCT and ICCG methods are selected for their computational efficiency, but their use has an associated trade-off – namely that, when solving the diffusion equation, it is necessary to assume monotonicity and positivity of positive-definite variables. Extreme gradients can lead to numerical artefacts in other parts of the model, *e.g.* thermal equilibration in the Spitzer-Harm model. Thus, POLLUX cannot simulate a true vacuum and to limit spatial gradients in the simulation 'vacuum' is defined by a minimum background mass density ρ_{bg} which, in the present work, was set as $\rho_{bg} = 10^{-7}$ ρ_{target}, where ρ_{target} is the target mass density given in Table 1. This leads to predictions of shock front formation at the leading edge of the plume for times later than ~20 ns, contrary to experimental observation. However, the plasma plume densities up until this point are much (10^2–$10^5\times$) higher than the background density. Thus hydrodynamic effects, which are the main source of error arising from assuming an unphysically high background density in the POLLUX modelling, will be very limited over these short time scales of ~20 ns.

Thus the POLLUX outputs are used in the following ways only. First, they provide insight into the evolving plume properties at early times, during the incident laser pulse. Second, these outputs guide the choice of input parameters (*e.g.* size, energy, mass, *etc.*) for modelling the subsequent adiabatic expansion of the plume (which is assumed to be either isothermal or isentropic) into vacuum. Following Stapleton *et al.*,[23] the former implies a spatially constant temperature and assumes density (ρ) and pressure profiles that are half-Gaussian in z and Gaussian in r at the start of the adiabatic modelling, while the isentropic formulation assumes a spatially dependent temperature profile and ρ and p profiles that are respectively half-ellipsoidal in z and ellipsoidal in r. Both assume that the expanding plume can be described by a self-similar model, implying linear velocity profiles, and the ideal gas equation with a constant adiabatic index γ. Full details of these alternative forms of adiabatic expansion model can be found in Stapleton *et al.*[23]

III RESULTS AND DISCUSSION

A Insights from the POLLUX calculations

Table I lists the parameters used in the POLLUX calculations. The temporal and spatial resolutions used in the reported calculations were 1 ps in t, 52.7 μm in r, and 11.5 μm and 33.0 μm in z in the plasma and target region, respectively. The small (1 ps) time step was chosen so that velocities of ~10^4 m s^{-1} could be dealt with on the 50 μm grid, *i.e*. the Courant number (C) of the simulation was much smaller than unity, satisfying the necessary condition for convergence. Trial simulations with a finer grid of 5 μm (in r) produced the same results, confirming convergence of our simulations.

The point $r = z = 0$ defines the centre of the interaction region on the target surface at the start of the laser pulse (which defines $t = 0$ in the present calculations). The laser pulse is assumed to be incident in the $-z$ direction and to have a Gaussian spatial and a near-Gaussian temporal intensity distribution with radius $R = 0.1$ mm at half maximum intensity and duration $\delta t = 8$ ns (FWHM). The total modelled laser pulse width is $2\times \delta t$ (16 ns), implying that the peak intensity is at $t = 8$ ns. As noted in Section II, the background mass density was set at $\rho_{bg} = 10^{-7}\rho_{target}$ (equivalent to a background pressure of ~0.21 mbar).

λ / nm	532 and 1064
δt (FWHM) / ns	8
R / mm	0.1
ϕ / GW cm^{-2}	20
$\rho_{target,\,Si}$ / g cm^{-3}	2.32
Reflectivity	0.374 (532 nm); 0.314 (1064 nm) [36,37]
ρ_{bg} / g cm^{-3}	2.32×10^{-7}

Table I. Parameters used in the POLLUX simulations.

The outputs from the POLLUX modelling are 2-D (z, r) spatial distributions of the mass density, ρ_i, the average charge state, q_i (where $q_i = 1$ is neutral, $q_i = 2$ is Si^+, *etc*.), the material expansion velocities orthogonal and transverse to the target surface (v_z and v_r) and the electron and heavy particle temperatures in each pixel i, at each time step. By way of illustration, Fig. 1 shows false colour $T_e(z, r)$ plots for $t = 5$, 10, 15, 25, 35 and 50 ns following PLA of Si in vacuum at $\lambda = 532$ nm, while Fig. 2 shows the calculated early time mass density and electron temperature distributions along the centre axis of this expanding plume, *i.e*. $\rho(z, r = 0; t)$ and $T_e(z, r = 0; t)$, respectively. The ρ distributions all peak at the substrate surface and decline rapidly with increasing z, while the calculated T_e distributions peak at $z > 0$. Even the $t = 15$ ns plots show a step at the leading edge, which becomes an obvious local

maximum at later t (see Fig. 1) and in calculations run with higher background mass densities. This reflects the early stages of shock front formation under the conditions of the simulation – for which there should be no analogue in the companion experiments. Henceforth, we therefore limit our discussion of POLLUX outputs to $t < 20$ ns. The corresponding $T_e(z, r; \lambda = 1064\text{ nm})$, $\rho(z, r; \lambda = 532$ nm), $\rho(z, r; \lambda = 1064$ nm), $q(z, r; \lambda = 532$ nm) and $q(z, r; \lambda = 1064$ nm) plots at $t = 5$, 10 and 15 ns for the PLA of Si in vacuum with the parameters specified in Table I are shown as Figs. S1–S5 in the supplementary information (SI).

The $\rho(z, r = 0; t = 5$ ns) distributions in the top left panel of Fig. 2 are very similar but, at later times, the LIPs formed by PLA of Si at 1064 nm clearly extend to larger z values, implying that 1064 nm PLA yields particles with higher velocity, v_z. 532 nm PLA yields the higher mass density, however. Figure 3(a) shows the predicted build-up of the total heavy particle population, P_h, during 532 and 1064 nm laser pulses along with the laser intensity (I) versus time profile assumed in the calculation. The population $p_{h,i}$ in pixel i at any given time t is derived from the calculated mass density (in excess of ρ_{bg}) divided by the relative atomic mass of Si, $A_r(\text{Si}) = 28.08$ u (*i.e.* the ejected material is assumed to be entirely atomic/ionic, not molecules or clusters). $P_h(t)$ is then obtained by integrating over the appropriate volume element, *i.e.* $\iint 2\pi r p_{h,i}(z,r)\mathrm{d}z\mathrm{d}r$. Figure 3(b) shows the time evolution of the average charge on the heavy particles (q_{av}) formed by PLA at the two wavelengths. These data are derived by spatial integration over the (population weighted) q_i distribution, *i.e.* $\iint 2\pi r p_{h,i}(z,r) q_i(z,r)\mathrm{d}z\mathrm{d}r$, at each t and then dividing by the corresponding $P_h(t)$ value. The build-up of the total electron yield P_e is then simply the product of P_h and $(q_{av} - 1)$ – shown in Fig. 3(c). The present POLLUX simulations show q_{av} increasing during the early part of the laser pulse but then decreasing as the incident intensity declines and the production rate of highly charged species (by IB absorption and thermal ionization) is overtaken by the rate of loss (by recombination).

Two effects (at least) contribute to the findings that 532 nm PLA causes greater material removal but the LIP formed by PLA at 1064 nm is 'hotter' – as measured by v_z, q_{av} or T_e. The absorption coefficient of Si is about two orders of magnitude larger at 532 nm than at 1064 nm,[37] resulting in more localised absorption, more concentrated target heating and higher material evaporation rates at the shorter wavelength. Target heating results in electron ejection, by thermionic and photo-emission processes. Electrons in the LIP gain energy by electron-photon coupling, yielding incipient plasma that can absorb further radiation by photoionization (PI) and, particularly, IB absorption.[14] The latter includes contributions from both electron-ion (e-i) and electron-neutral (e-n) interactions, described by the respective absorption coefficients [38]

$$\alpha_{\mathrm{e-i}} = \frac{4}{3}\left[1 - \exp\left(-\frac{hc}{\lambda T_{\mathrm{e}}}\right)\right]\left(\frac{2\pi}{3mT_{\mathrm{e}}}\right)^{1/2}\frac{e^6\lambda^3 N_{\mathrm{e}}}{mhc^4}\left(\sum_{Z=1}(Z-1)^2 N_{\mathrm{Si}^z}\right) \quad (1)$$

$$\alpha_{\mathrm{e-n}} = \left[1 - \exp\left(-\frac{hc}{\lambda T_{\mathrm{e}}}\right)\right] N_{\mathrm{e}} Q_{\mathrm{e-Si}} N_{\mathrm{Si^I}} \ . \quad (2)$$

Z in eq. (1) defines the charge state, using the conventional spectroscopic notation that Si^I is a neutral Si atom, Si^{II} represents Si^+, *etc*. (the q values output by POLLUX are thus equivalent to Z), $Q_{\mathrm{e-Si}}$ in eq. (2) is the photoabsorption cross-section, and all other symbols have their usual meanings. The $\left(1 - \exp(-hc/\lambda T_{\mathrm{e}})\right)$ term in each equation accommodates the contribution from stimulated emission. The magnitude of this term decreases with increasing wavelength, but it is a weak λ dependence. This is the only λ-dependent contribution to $\alpha_{\mathrm{e-n}}$ and, since the present work is focused on wavelength dependent differences in the production and properties of LIPs, we henceforth concentrate on e-i IB absorption (eq. (1)). Any λ dependence in the $\left(1 - \exp(-hc/\lambda T_{\mathrm{e}})\right)$ term in $\alpha_{\mathrm{e-i}}$ will be dwarfed by the effect of the λ^3 term; IB absorption accounts for the 'hotter' LIP formed by PLA at 1064 nm (*cf.* 532 nm).

The model outputs give some further insights into when and where the incident radiation is absorbed during the laser pulse. Given the electron densities implicit in Fig. 3(c), a stage will be reached when the local plasma frequency in the developing LIP matches the incident laser frequency (*i.e*. the critical plasma density: n_{c} ~1.2×10^{-2} g cm^{-3} for 1064 nm with $q_{\mathrm{av}} = 4$; n_{c} ~6.1×10^{-2} g cm^{-3} for 532 nm with $q_{\mathrm{av}} = 3$) and the plasma reflectivity increases rapidly. The LIP then starts to act as a plasma shutter, attenuating the later part of the incident pulse at small z and on the target surface. Some of the reflected radiation will be absorbed on its way out of the plasma. Such effects are included in the POLLUX modelling (albeit only in a semi-quantitative manner); clearly, they will be more important at 1064 nm, and are another contributory factor to the lower yield of ablated material when exciting at the longer wavelength. They also contribute to the obvious differences in the spatial distributions of ρ (figs. S2 and S3, which depend on laser-target interaction) compared to those for T_{e} or q (figs. 1, S1, S4 and S5, which reflect energy uptake in the plume).

Wavelength / nm	532	1064
z extent / μm	425	575
Expansion velocity in z / m s^{-1}	2.4×10^4	3.3×10^4
r extent / μm	200	200
Expansion velocity in r / m s^{-1}	0.9×10^4	1.4×10^4
Energy content / mJ	7.5	10.2
Mass content / ng	39	31

Table II. Size, velocity, energy and mass content of LIPs at t = 15 ns following 532 nm and 1064 nm PLA of a Si target predicted by POLLUX calculation using the parameters listed in Table 1.

For future reference, Table II lists the sizes and expansion velocities (in the z and r dimensions), energy and mass contents of the 532 nm and 1064 nm LIPs predicted by the POLLUX modelling at t = 15 ns using the parameters listed in Table I. These parameters are the input variables for the adiabatic expansion models used later. The density and temperature profiles for the initial conditions of the adiabatic expansion models are assumed to be half-Gaussian (density) and constant (temperature) for the isothermal model, and elliptical (density and temperature) for the isentropic model. The temperature for the isothermal model is derived from the plume energy and mass content, assuming an ideal gas. As a further point of context, the model parameters in Table I equate to incident pulse energies of ~100 mJ, implying ~10% energy conversion into plume excitation. We also note that the ρ and N_e values predicted in the core of the LIP at t = 15 ns are >>10^{24} m^{-3}, thereby satisfying the McWhirter criterion [39] and validating the use of POLLUX (which assumes LTE) to simulate the early time plume dynamics. As shown before [15] and later in this study, however, the validity of assuming LTE must break down at later times as the plume expands into vacuum.

B Insights from time-gated, spatially and spectrally resolved optical emission imaging

Figure 4 shows spatially and spectrally resolved $I(z, \lambda; t)$ images of emission in the range $452 \leq \lambda \leq 487$ nm measured at t = 60, 90 and 120 ns after the start of the pulsed irradiation of a Si target in vacuum at 532 and 1064 nm (left and right panels, respectively). This spectral region, which also featured in our first demonstration of the use of time-gated, spatially resolved emission imaging methods to determine electron characteristics within evolving LIPs,[15] is ideal for tracking the propagation of Si^{III} and Si^{IV} emitters. Weak Si^{II} emissions associated with the $3s^27f^1 \rightarrow 3s^24d^1$ and $3s^28g^1 \rightarrow 3s^24f^1$ transitions at, respectively, 462.1 and 467.3 nm are also discernible at small z, most clearly in the 532 nm LIP at early t, but the monitored wavelength range contains no transitions due to Si^I species.

The experiment allows us to map the temporal evolution of specific ion charge state distributions (and the electron characteristics in the locality of those ions). The spatial fractionation of the Si^{III} and Si^{IV} emitters is obvious in these images, as are the similar spatial distributions of all emissions emanating from a given charge state.[15] The same spectral features are observed at both excitation wavelengths, but the emissions from the more highly charged (Si^{IV}) ions appear with greater relative intensity in the 1064 nm images and, at any given t, each emission within the 1064 nm LIP extends to larger z than in the 532 nm LIP. Both observations accord with the POLLUX predictions: e-i IB absorption is greater at the longer excitation wavelength, resulting in a faster plume expansion (recall Fig. 2) and a higher average degree of ionization (recall Fig. 3).

The temporal and spatial variations of the Stark-broadened line shapes extracted from the $I(z, \lambda; t)$ images were analysed using a modified Saha equation based on a Druyvesteyn (rather than a Maxwellian) EEDF, *i.e.* with no assumptions about the applicability (or not) of LTE.[15,16] Several previous works have addressed the validity of assuming LTE in the case of LIPs formed at ambient pressure,[40,41] but such an assumption clearly cannot be valid for the later stages of a LIP expanding into vacuum. As previously, the profile of each Si^{III} and Si^{IV} transition of interest was predicted for numerous combinations of N_e and T_e using the established w and d Stark parameters[15] and the z-dependent N_e and T_e values determined as the combinations that gave the smallest sum of squared differences (SSD) when compared with experiment (after convolving the predicted spectrum with the instrumental line shape).

Figs. 5 and 6 show, respectively, the $N_e(z)$ and $T_e(z)$ values derived from such analysis of Stark broadened line shapes in images of the emission from LIPs formed by PLA at 1064 and 532 nm recorded at t = 60, 90, and 120 ns. The derived N_e values peak at the smallest z at which emission can be observed and, at any given t, these peak values are larger in the 532 nm LIP than in the 1064 nm LIP. However, the z-dependent decline in N_e is steeper in the 532 nm LIP, so that the reverse holds further from the target (*i.e.* $N_e^{1064} > N_e^{532}$ at $z > 2$ mm at $t = 60$ ns, and at $z > 3.5$ mm at $t = 90$ ns). These trends accord with expectations based on the POLLUX modelling: e-i IB absorption is more important at 1064 nm, and the LIP is thus more highly ionised at large z and has a higher expansion velocity. The T_e values returned from analysis of the Si^{III} and Si^{IV} line shapes decline with increasing z and t and are <1 eV over most of the range probed in this experiment. These $N_e(z, \lambda; t)$ and $T_e(z, \lambda; t)$ trends are compared with predictions from two limiting forms of an adiabatic plume expansion model in section IIIC.

The POLLUX calculations suggest that Si^{III} and Si^{IV} cations might be fairly representative of the average charge state in the core of the plasma during the laser excitation, but to what extent is this true at later times? The plasma expands, cools and, as Fig. 4 shows, the emissions from different charge states become spatially separated. Three-body collisional and/or radiative electron-ion recombination processes (wherein an additional electron or a photon ensures energy and momentum conservation) are major particle loss mechanisms during this expansion phase, with the former dominating under the higher density conditions prevailing at early times.[42] Thus we might anticipate higher three-body recombination rates in the LIP produced at 532 nm, which may be another contributory factor to the reduced relative intensity of the emission from Si^{IV} cations in the 532 nm LIP, *cf.* the 1064 nm LIP (Fig. 4).

Other factors that merit comment are the charge-dependent spatial fractionation of the different emitting species, and the possible mechanisms by which these emitting species are formed. Many prior studies of PLA plumes have noted that ions in different charge states propagate with different velocities. As here, these studies typically find that more highly charged ions expand faster.[11,43] This is generally attributed to space charge effects, though the detailed mechanism is often less clear. For example,

Cowin and coworkers [44,45] proposed a space-charge acceleration model, wherein the initial ejection of electrons in the earliest stages of the ablation process encourages formation of an electric field gradient between the foremost electrons in the plume and the (net positively charged) target surface, which would have the effect of accelerating positively charged species within the plume, to extents that depend on their charge state. Such a mechanism could be important under conditions of much lower irradiance, but the plasmas formed in the present work are surely too dense (and the Debye lengths too short) for this particular polarization to be responsible for the observed fractionation.

The POLLUX modelling and other hydrodynamics based models [46,47] suggest an alternative space-charge based picture that is capable of explaining many of the present observations. Inspection of the early time $T_e(z, r; t)$ and $q(z, r; t)$ plots in Figs. 1, S1, S4 and S5 shows that the q profiles consistently peak further from the target, implying that the average charge state of the material in the plume during the laser excitation maximizes towards the leading edge (*i.e.* the more highly charged particles have higher velocities). This is inevitable if e-i IB absorption is the dominant laser-plume interaction and the plume is (or is tending towards being) optically dense, but it is not clear that this alone should result in the very different Si^{III} and Si^{IV} expansion velocities observed experimentally. These ions are accompanied by electrons, at densities sufficient to ensure approximate local charge neutrality. These electrons will have a spread of velocities. Some of the hottest electrons will be propagating at the very front of, and escape from, the expanding plume.[48] This charge separation between the hot electrons and the most highly charged ions at the front of the plume is a plausible explanation for the spatial fractionation of the cations observed in the present experiments, though it is not clear to what extent this is enhanced by e-i IB absorption during the laser pulse, or if the most highly charged ions are able to "ride the wave" of space charge created by the continual escape of hot electrons. Whatever the detailed acceleration mechanism, it appears that it is only because the ions travel together with an associated "packet" of electrons that quasi-neutrality is maintained and the ions are relatively free to expand at their final velocities once the laser excitation is finished.

We now address the mechanism(s) responsible for the optical emission observed after cessation of the laser pulse. The emitting states of Si^{3+} observed in the present work have total energies of ~40 eV (relative to the Si^{IV} ground state) and ~98 eV relative to the ground state of neutral Si. Si^{V} is a closed shell species, isoelectronic with Ne, with a much higher ionization potential (166.8 eV, defined relative to the Si^{V} ground state).[49] Application of the Rydberg formula suggests that $2p^5 7l'^1 \rightarrow 2p^5 6l''^1$ transitions involving high l' and l'' (*i.e.* between states lying ~160 eV above the Si^{V} ground state) would lie at the long wavelength end of the range spanned in Fig. 4, but no such emissions were discerned in the present study. Nonetheless, even if we restrict discussion to the observed emitting states of Si^{3+}, less than 1 in 10^{30} electrons in a Druyvesteyn EEDF with T_e ~1 eV would have the necessary ~40 eV energy required

for direct electron impact excitation of a ground state Si^{3+} ion to be a plausible mechanism for forming the observed emitting species.

Three body collisional recombination and/or radiative recombination are therefore seen as more likely routes to forming the more highly charged species observed towards the front of the plume. Such recombinations have the effect of converting an electron plus an ion with charge Z into an ion with charge (Z−1). The energy mismatch is least if the electron enters a high nl Rydberg orbital. The excited $Si^{(Z-1)+}$ species that result will decay by collisional relaxation and/or by emitting a photon. The selection rules for the radiative decay of a state involving a Rydberg electron with a high l quantum number dictate a sequence of transitions (a radiative cascade), one of more of which would be likely to fall in the visible region monitored in the present work. Such an explanation has been advanced previously [50,51] to account for the persistence of C and C^+ emissions following 193 nm PLA of graphite and of Zn^+ emissions from the 193 nm PLA of ZnO (both in vacuum) to times well beyond the radiative lifetimes of the monitored excited levels. Clearly, the probabilities of such recombination processes decrease with increasing z and/or t, as the plume expands and the collision frequency declines. Thus one consequence of such a mechanism is that properties like the expansion velocity v_z derived through analysis of a given $Si^{(Z-1)+}$ emission may actually be more characteristic of the Coulombic and hydrodynamic forces acting on the heavy particle at earlier times within the expansion, when it was a Si^{Z+} (or even more highly charged) cation. From the perspective of the electron characteristics, however, spectroscopy leaves no ambiguity about the identity of the species that is being subjected to Stark broadening, or of the electron characteristics derived therefrom.

C. Insights from numerical modelling of the adiabatic expansion of these LIPs.

Figure 5 compares spatially resolved $N_e(z)$ measurements at t = 60, 90 and 120 ns after the start of the pulsed irradiation of a Si target in vacuum with the isentropic (green) and isothermal (red) adiabatic expansion model predictions at 532 and 1064 (left and right panels, respectively). The isothermal model appears to provide the better match to the experimental data, both in terms of the z profile and the absolute values of N_e. The agreement is far from perfect, however. At both wavelengths, the predicted gradients in $N_e(z)$ are shallower than observed experimentally, *i.e.* the isothermal model overestimates the size of the plasma plume. The isentropic model, in contrast, seriously underestimates the plume size. Further, the isentropic model predicts a $N_e(z)$ profile that drops steeply at the plume edge, very unlike the gradual decrease, up until the detection limit of the diagnostic, that is observed experimentally.

At this point it is worth reiterating that these adiabatic model predictions involve no fitting parameters, nor any inputs from the experimental data; they are independent of the experimental results.

Thus the qualitative, and to some extent quantitative, match between the $N_e(z)$ predictions from the isothermal adiabatic model and the experimental data is encouraging, particularly in light of the assumptions included in the modelling, *e.g.* Gaussian initial conditions and no recombination in the plume. That the isothermal model matches the present experimental data better than the isentropic model accords with criteria established by Stapleton *et al.*,[23] wherein the expansion dynamics are predicted to reflect the ratio of the initial extent of the plasma in the r and z directions (which links back to the laser spot size on the target). Isothermal behaviour is predicted if this ratio is less than or close to unity, while isentropic behaviour prevails for ratios well above unity. These ratios in the present case are ~0.47 and ~0.35 for λ = 532 and 1064 nm, respectively (Table II).

Figure 6 shows the corresponding spatially resolved $T_e(z)$ data at t = 60, 90 and 120 ns after the start of the pulsed irradiation of a Si target in vacuum – again with the adiabatic expansion model predictions at λ = 532 and 1064 nm (left and right panels, respectively) assuming isentropic (green) and isothermal (red) starting conditions. Neither model reproduces the experimental data well. Notwithstanding the fact that the isothermal model provided a reasonable match to the measured $N_e(z)$ profiles, the isothermal assumption is clearly invalid as the measured $T_e(z)$ profiles all show at least an order of magnitude decline across the measured range. Again, the isentropic model fails to reproduce the shape of the observed profiles.

Though the isothermal variant of the adiabatic expansion model provides the better match to the experimental N_e data, it clearly does not capture all the relevant processes. This is illustrated most strikingly in Fig. 6, but also in Fig. 5. The experimental data in the latter figure, at both wavelengths and especially at later t, suggest a 'step-like' $N_e(z)$ profile with a higher (and relatively constant) density closer to the surface (z < 3 mm) and a lower density at z > 3 mm. The isothermal model predicts significant expansion at such late times, resulting in a relatively flat profile across the entire observation window (z = 0 - 5 mm). Thus the measured profiles hint that the plumes might involve two (distinct) isothermal contributions – one with a higher temperature and expansion velocity that is revealed in the $N_e(z)$ profiles at z > 3 mm and another with a lower temperature and expansion velocity that dominates the observed profile at z < 3 mm. The t = 120 ns data in Fig. 6, which show similar step-like $T_e(z)$ profiles, provide similar hints of a two-temperature plasma.

We now consider the validity of assuming either isothermal or isentropic initial conditions. Figure 7 shows the $N_e(z)$ and $T_e(z)$ profiles predicted by the POLLUX calculations at t = 15 ns (*i.e.* at the end of the laser pulse) for both wavelengths. The centres of the $N_e(z)$ profiles (0.1 < z < 0.55 mm for 1064 and 0.1 < z < 0.35 for 532 nm) approximate the half-Gaussian shape assumed in the isothermal model, but there is excess electron density close to the target (z < 0.05 mm) and the density drops much more steeply at the leading edge of the plume than predicted by a half-Gaussian function. Nonetheless, for the bulk of the plasma, a half-Gaussian (isothermal) assumption seems reasonable. The $T_e(z)$ profiles

predicted by the POLLUX calculations at t = 15 ns show a range of temperatures (~4-8 eV for λ = 1064 nm and ~3-6 eV for λ = 532 nm), however, which are obviously incompatible with the constant temperature profile implicit in the isothermal model.

The sharp drops in T_e predicted by the POLLUX calculations close to the target surface (z < 0.1 mm) and near the leading edge of the plume (Fig. 7) merit comment. The former, and the predicted increased electron density (and mass density (Fig. 2)) in the same z < 0.1 mm region (at t = 15 ns), implies a relatively cold and dense plasma close to the target surface and a hotter, expanding plasma plume at larger z. Such observations could all be consistent with the plasma-shutter scenario outlined earlier. The leading edge of the laser pulse initiates ablation of some material at relatively low temperature, which is subsequently heated via IB. Then, when the local plasma frequency in the developing LIP matches the incident laser frequency (the critical plasma density), the plasma reflectivity increases rapidly. The plasma between the target surface and the region of critical density is shielded from the remainder of the laser pulse and thus does not heat further, whereas the plasma at larger z experiences further IB absorption and heating through the remainder of the pulse. Such a scenario would result in a hotter, IB-heated exterior around a cooler, partially shielded region close to the target surface. However, we also note that the LIPs expand during the laser pulse, and the plume densities decrease with t. The ρ vs z plots in Fig. 2 show densities of order 10^{-2}–10^{-3} g cm^{-3} at z < 0.1 mm. These are below the critical densities (n_c ~4.6×10^{-2} g cm^{-3} at λ = 1064 nm and 1.9×10^{-1} g cm^{-3} for λ = 532 nm), implying that the shielded region of the embryonic plasma must be localised very close to the target (z less than ~0.02 mm). We also note that heat conduction from the plasma to the solid target could contribute to a decrease in plasma temperature close to the target, but it is not possible from the current simulations to determine the relative importance this effect.

The predicted (and observed) drop in T_e near the leading edge of the plume can also be understood in terms of a two-temperature picture. The early stage (first few ns) of the PLA process results in a small plasma close to the target surface with a moderate temperature, T_e ~3-4 eV (see Figs. 1 and S1). The parts of this plasma with greatest expansion velocity v_z will form the leading edge of the expanding plume. The electron and ion densities at this edge are much lower than in the core region near the target, and these differences in charged species density will map through into the relative efficiencies of IB absorption (eqs. (1) and (2)) – which will be much lower at the leading edge. Thus we should expect the periphery of the plume to expand during the laser pulse with a relatively constant T_e, while the denser core of the plasma experiences greater IB heating from the remainder of the pulse. Again, such expectations accord with the POLLUX outputs (Fig. 2), which show a clear increase in T_e in the core region (at z ~0.05 mm) between t = 5 and 10 ns. Material in this region of the developing plasma has a lower expansion velocity than material at the leading edge, so over this small time range the peak of the T_e distribution appears relatively stationary in z. After the peak of the laser pulse, and

the plasma heating from IB absorption reduces (and eventually stops), we observe the overlapping expansion of two regions of plasma – one near the leading edge of the plume, characterised by higher v_z but relatively low T_e, the other, nearer the target, with higher density and temperature. Such a two-temperature picture provides a rationale for the predicted ρ and T_e profiles at t = 15 ns (Fig. 2) and the experimental profiles at later times (Fig. 5). Clearly, further investigations using both POLLUX and two-temperature adiabatic modelling would be needed to verify this hypothesis but Figs. 7 (and 5 and 6) serve to highlight some of the issues associated with using adiabatic models to describe expanding LIPs formed with ns laser excitation. Neither isothermal nor isentropic assumptions seem justified in any accurate description of the expansion.

IV CONCLUSIONS

The wavelength dependence of LIPs formed by 1064 nm and 532 nm ablation of a Si target in vacuum using ns laser pulses of similar irradiance has been investigated by simulation, using both hydrodynamic (POLLUX) and adiabatic models, and experimentally, by measurement and analysis of individual line shapes in time-gated, spatially-resolved $I(z, \lambda; t)$ images of the plume emission. Given comparable laser parameters, the POLLUX modelling shows that 532 nm irradiation results in greater material ablation, that the LIP formed by 1064 nm excitation is characterised by a higher average charge state and expands faster, and that the emerging plasma can attenuate the laser-target interaction in the later stages of the pulse. Simply dividing the laser pulse energy by an assumed interaction area should be expected to provide a poor (upper limit) estimate of the fluence incident on the target. Analysis of Stark-broadened line shapes allows mapping of the evolving absolute N_e and T_e values in the LIPs formed by both 532 nm and 1064 nm irradiation, out to t ~120 ns. The data confirm the importance of electron-ion IB absorption in coupling the incident laser radiation into the emergent plasma, but the details of this interaction, and the ways it affects the electron properties, the distribution of ion charge states and the spatial distributions of the ions and electrons within the evolving LIP are all shown to be sensitive to the choice of excitation wavelength.

The POLLUX modelling of the laser-target and laser-plume interactions during the incident pulse provided inputs for an adiabatic expansion model that allows direct comparison with the experimental data, without recourse to fitting parameters or any inputs from the experimental data. Assuming isothermal conditions for the starting plasma in the adiabatic modelling gives a reasonable fit to the observed $N_e(z)$ profile, but the experimental $T_e(z)$ profile is clearly not constant (as would be required in any isothermal model). The alternative isentropic starting assumption for the adiabatic expansion model did not reproduce either the experimental $T_e(z)$ or $N_e(z)$ profiles. Further analysis of the POLLUX predictions highlights some of the shortcomings of the adiabatic expansion modelling

using either isothermal or isentropic initial conditions. The density profile is not strictly half-Gaussian, with excess density very close to the target surface and a sharper drop-off at the leading edge of the plume. Neither is the temperature profile constant, with lower temperatures close to the target and near the leading edge. Clearly, more realistic density and temperature profiles – such as could be predicted by POLLUX, for example – are needed as initial conditions if an adiabatic expansion model is to provide a better match to experimental results. Alternatively, a fully computational approach (*e.g.* a Computational Fluid Dynamics (CFD) model) could be pursued wherein the adiabatic expansion is also described numerically.

SUPPLEMENTARY MATERIAL

See **supplementary material** for false colour (z, r) plots of the following plume properties at t = 5, 10 and 15 ns predicted by the POLLUX calculations following PLA of Si in vacuum: T_e at λ = 1064 nm; ρ at λ = 532 and 1064 nm; q at λ = 532 and 1064 nm.

ACKNOWLEDGEMENTS

The authors are grateful to EPSRC for financial support of work in the Universities of Bristol and York via the Intelligent Manufacturing Initiative (EP/K018388/1), and to the University of Bristol and the China Scholarship Council for a postgraduate scholarship (to HL). HL and MNRA are very grateful to Dr Benjamin S Truscott for his help and interest in all aspects of the experimental work reported herein. HL acknowledge helpful advice regarding the POLLUX code and discussions with Dr. Andrew Rossall and all the support provided by Ph.D. candidate Ms Xu Han.

Data accessibility: Data are available at the University of Bristol data repository, at DOI: 10.5523/bris.1whkrkaw7gibs2t786d7mbqcw8.

Figure captions

Figure 1

2-D(z, r) spatial distributions of T_e in the LIPs formed by PLA of a Si target at 532 nm calculated at t = 5, 10, 15, 25, 35 and 50 ns using the parameters listed in Table I. The vertical and horizontal axes in each plot are z, the distance normal to the target surface (located at z = 0) and the radial distance r. The T_e scales (linear, in eV) are defined by the false colour scheme shown to the immediate right of each plot.

Figure 2

Mass density $\rho(z, r = 0)$ (left) and electron temperature $T_e(z, r = 0)$ (right) distributions at t = 5, 10, 15 ns in LIPs formed by 532 nm (black) and 1064 nm (red) PLA of a Si target predicted using the POLLUX code and the parameters listed in Table 1. The horizontal lines in the left-hand panels show the ρ_{bg} value used in these simulations.

Figure 3

Temporal distributions of: (a) the laser pulse intensity I assumed in the modelling (blue curve) and the calculated total heavy species population, P_h, in the LIPs formed by 532 and 1064 nm irradiation (black and red traces, respectively); (b) the average charge state, q_{av}, of the heavy particles; and (c) the total electron yield, P_e, in the respective plumes.

Figure 4

Spatially resolved optical emission spectra measured at t = 60, 90 and 120 ns over the wavelength range $452 < \lambda < 487$ nm following 532 nm (left) and 1064 nm (right) PLA of a Si target (the surface of which is located at $z = 0$) in vacuum using an irradiance ϕ = 20 GW cm^{-2}. The logarithmic false colour intensity scale is shown to the right of each row.

Figure 5

z-dependent N_e values (in m^{-3}) derived from analysis of spatially resolved Si^{III} and Si^{IV} line shapes measured at t = 60, 90 and 120 ns (black lines, top, middle and bottom rows, respectively) following 532 nm (left) and 1064 nm (right) PLA of a Si target in vacuum at $\phi \approx$ 20 GW cm^{-2}, together with the isentropic (green) and isothermal (red) adiabatic expansion model predictions using the POLLUX outputs (Table II) as initial input parameters.

Figure 6

z-dependent T_e values (in eV) derived from analysis of spatially resolved Si^{III} and Si^{IV} line shapes measured at t = 60, 90 and 120 ns (black lines, top, middle and bottom rows, respectively) following

532 nm (left) and 1064 nm (right) PLA of a Si target in vacuum at $\phi \approx 20$ GW cm^{-2}, together with the isentropic (green) and isothermal (red) adiabatic expansion model predictions using the POLLUX outputs (Table II) as initial input parameters.

Figure 7

POLLUX calculations of z-dependent T_e (black) and N_e (red) at the end of the laser pulse (t = 15 ns) for 532 nm (left) and 1064 nm (right) PLA of a Si target. These conditions mark the input for the adiabatic expansion model (see Table II).

Figure 1

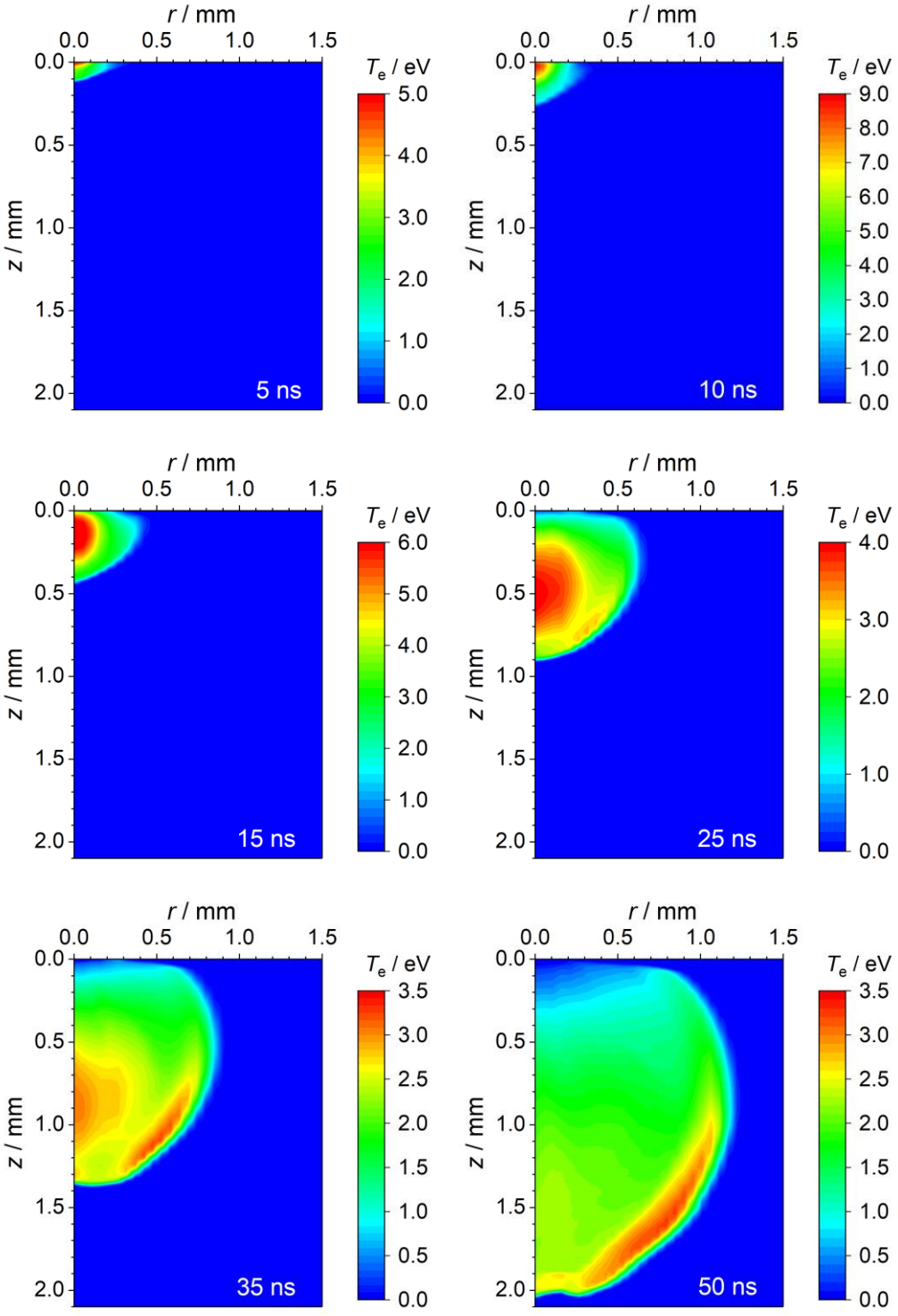

Figure 2

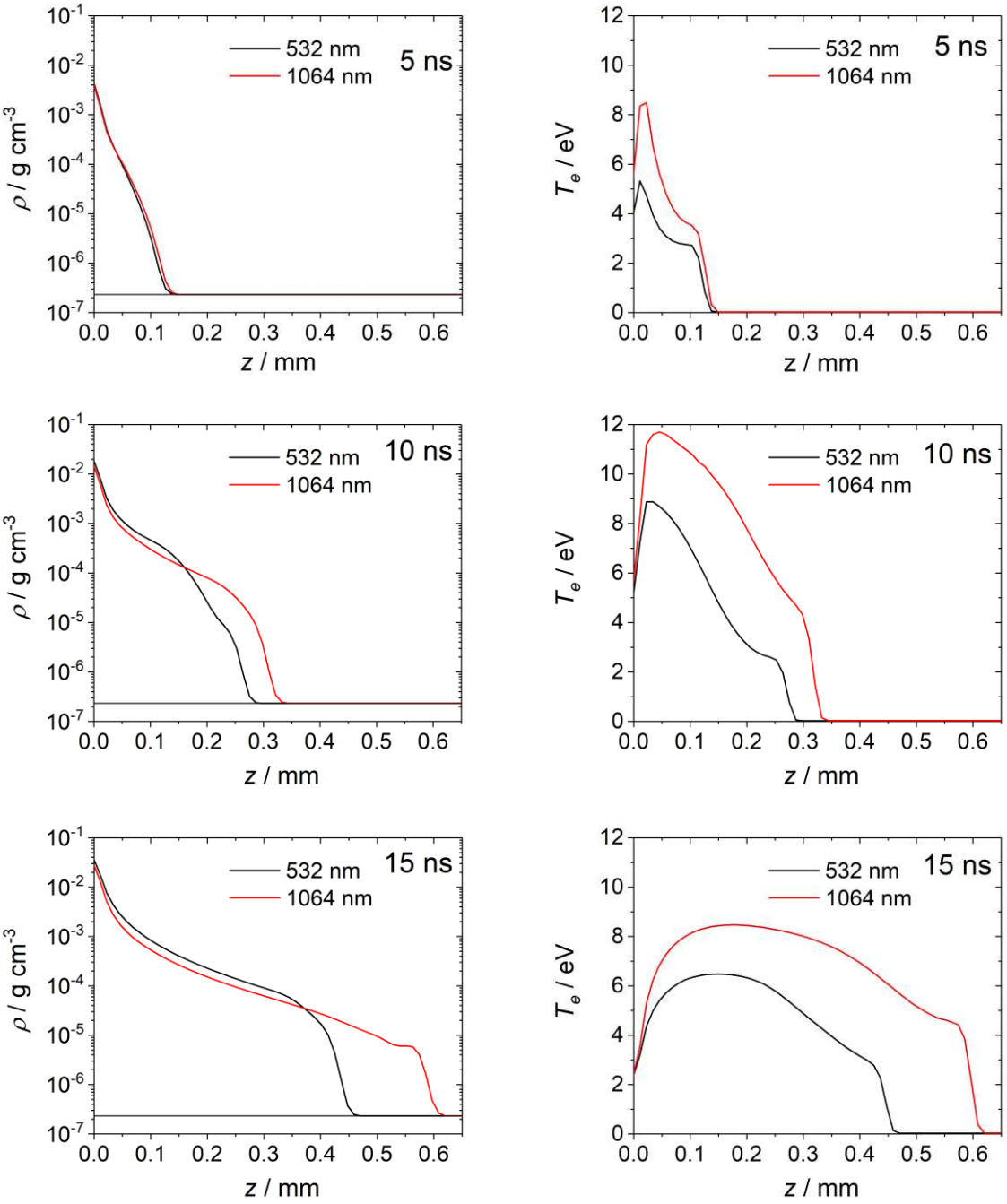

Figure 3

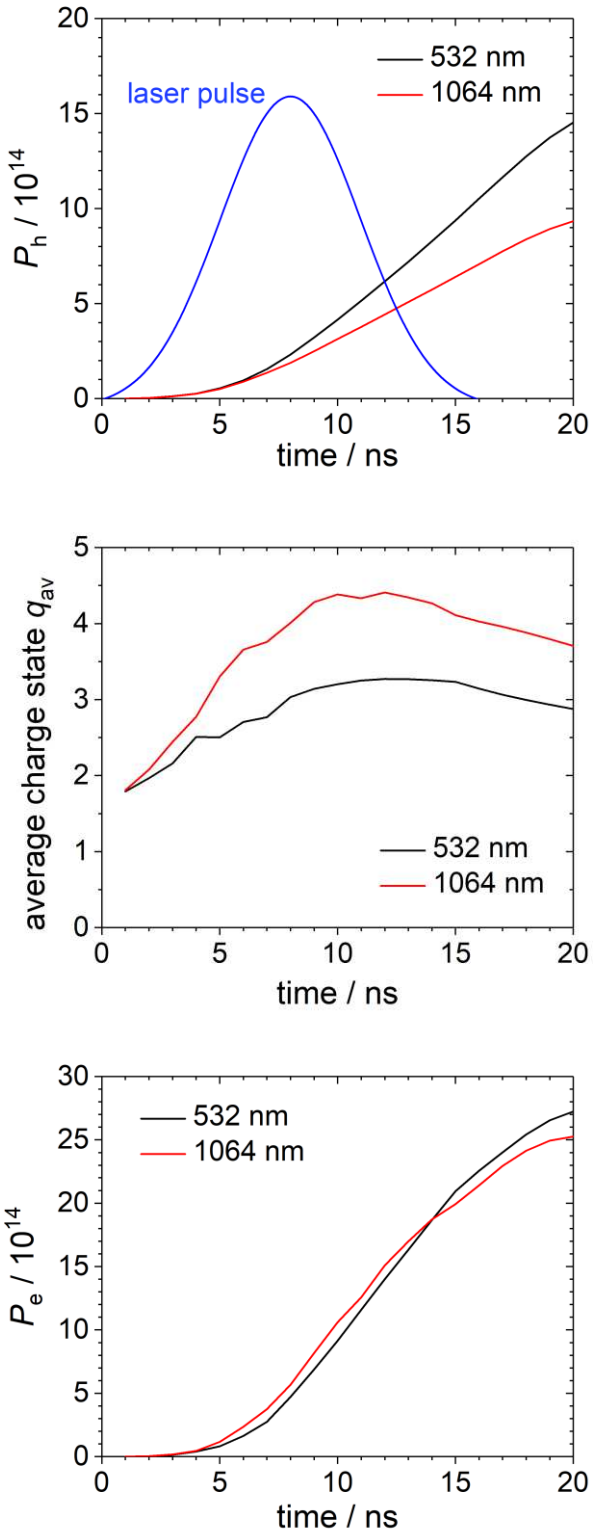
laser pulse
532 nm
1064 nm
P_h / 10^{14}
time / ns
average charge state q_{av}
532 nm
1064 nm
time / ns
P_e / 10^{14}
532 nm
1064 nm
time / ns

Figure 4

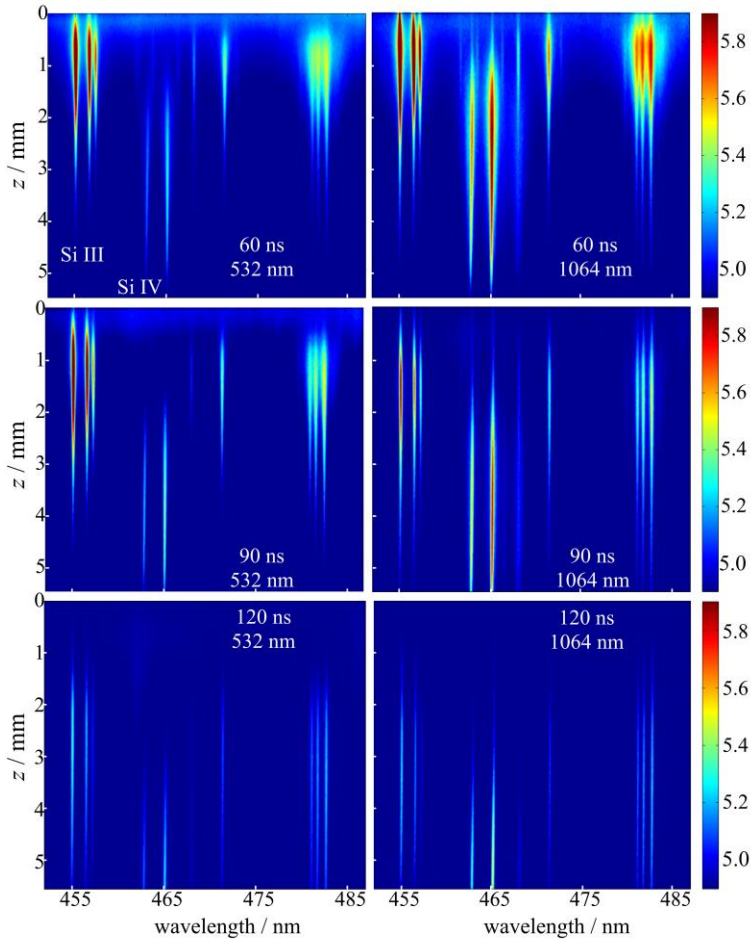
Si III
Si IV
60 ns
532 nm
60 ns
1064 nm
90 ns
532 nm
90 ns
1064 nm
120 ns
532 nm
120 ns
1064 nm
z / mm
wavelength / nm
0
1
2
3
4
5
455
465
475
485
5.8
5.6
5.4
5.2
5.0

Figure 5

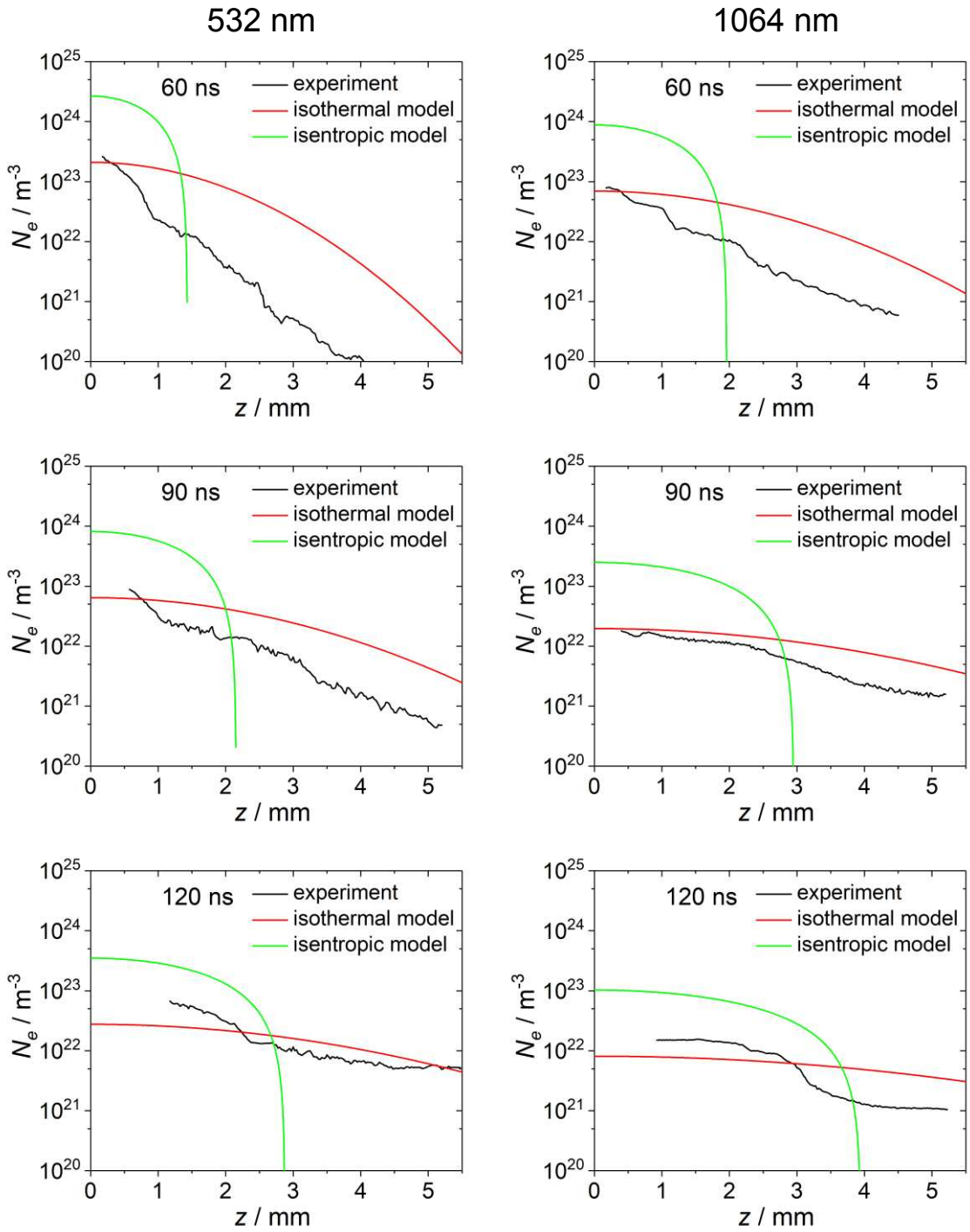
532 nm
1064 nm
60 ns
90 ns
120 ns
experiment
isothermal model
isentropic model
N_e / m^{-3}
z / mm

Figure 6

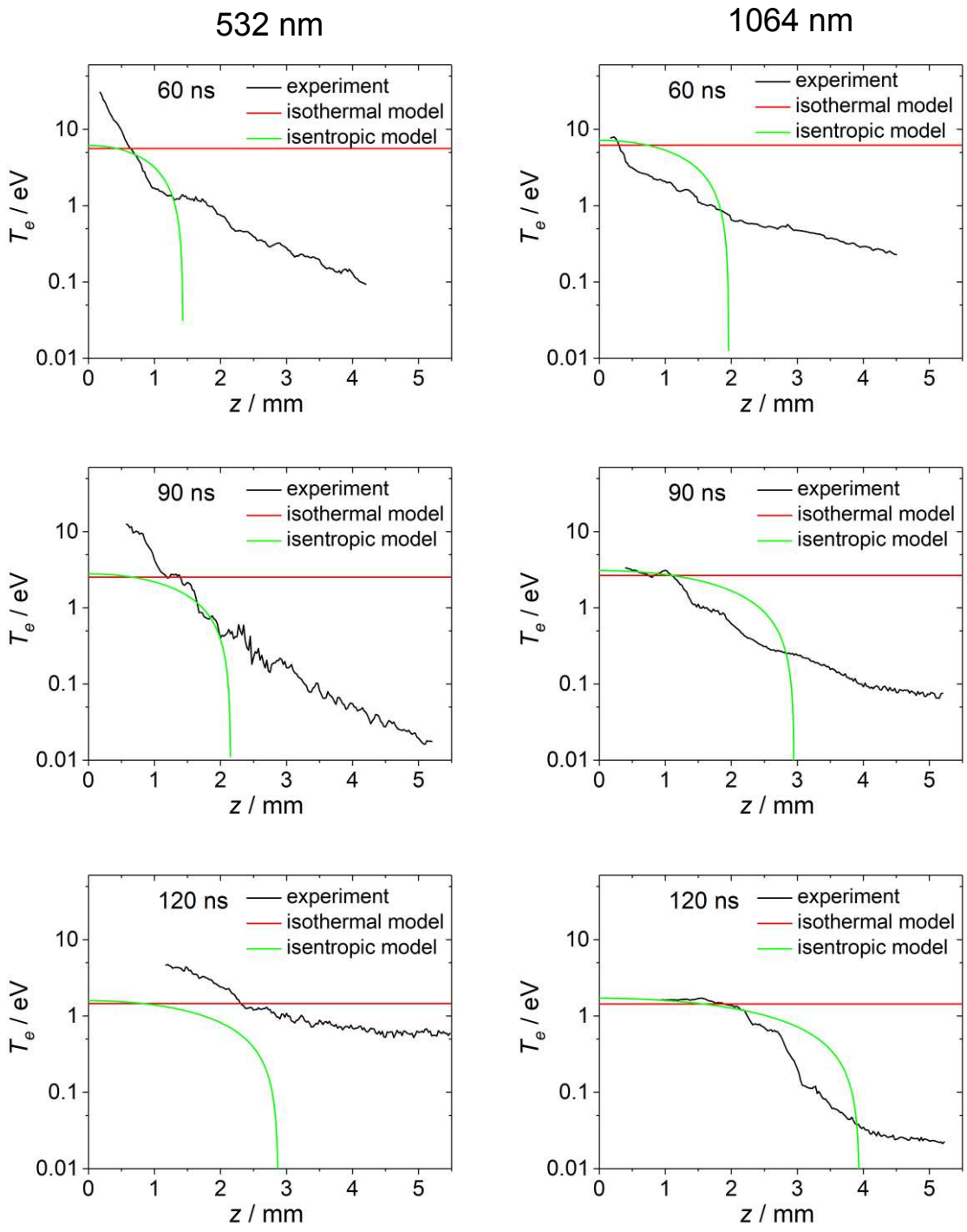
532 nm
1064 nm
60 ns
90 ns
120 ns
experiment
isothermal model
isentropic model
T_e / eV
z / mm

Figure 7

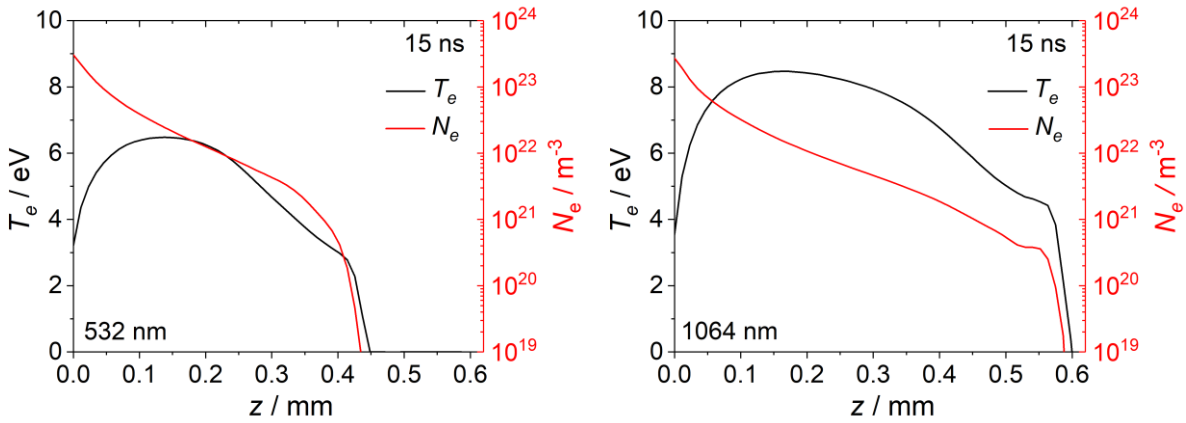

References

[1] M.A. Shannon, X.L. Mao, A. Fernandez, W.T. Chan and R.E. Russo, Anal. Chem. **67**, 4522-4529 (1995).

[2] B. LeDrogoff, J. Margot, F. Vidal, S. Laville, M. Chaker, M. Sabsabi, T.W. Johnston and O. Barthélemy, Plasma Sources Sci. Technol. **13**, 223-230 (2004).

[3] H. Borchert, K. Daree and M. Hugenschmidt, J. Phys. D Appl. Phys. **38**, 300-305 (2005).

[4] S.S. Harilal, R.W. Coons, P. Hough and A. Hassanein, Appl. Phys. Lett. **95**, 221501 (2009).

[5] R. Fabbro, E. Fabre, F. Amiranoff, C. Garbanlabaune, J. Virmont, M. Weinfeld and C.E. Max, Phys. Rev. A **26**, 2289-2292 (1982).

[6] X.L. Mao, A.C. Ciocan, O.V. Borisov and R.E. Russo, Appl. Surf. Sci. **127,** 262-268 (1998).

[7] I. Horn, M. Guillong and D. Gunther, Appl. Surf. Sci. **182**, 91-102 (2001).

[8] G. Abdellatif and H. Imam, Spectrochim. Acta B **57**, 1155-1165 (2002).

[9] O. Barthélemy, J. Margot, M. Chaker, M. Sabsabi, F. Vidal, T. W. Johnston, S. Laville and B. LeDrogoff, Spectrochim. Acta B **60**, 905-914 (2005).

[10] N.M. Shaikh, S. Hafeez, B. Rashid, S. Mahmood. and M.A. Baig, J. Phys. D Appl. Phys. **39,** 4377-4385 (2006).

[11] S.S. Harilal, T. Sizyuk, D. Hassanein, D. Campos, P. Hough and V. Sizyuk, J. Appl. Phys. **109**, 063306 (2011).

[12] T. Moscicki, J. Hoffman and Z. Szymanski, J. Appl. Phys. **114**, 083306 (2013).

[13] A.E. Hussein, P.K. Diwakar, S.S. Harilal and A. Hassanein, J. Appl. Phys. **113**, 143305 (2013).

[14] A. Bogaerts, Z.Y. Chen, R. Gijbels and A. Vertes, Spectrochim. Acta B **58**, 1867-1893 (2003).

[15] H. Liu, B.S. Truscott and M.N.R. Ashfold, Plasma Sources Sci. Technol. **25**, 015006 (2016).

[16] H. Liu, B.S. Truscott and M.N.R. Ashfold, Sci. Rep. **6**, 25609 (2016).

[17] W. Marine, N.M. Bulgakova, L. Patrone and I. Ozerov, J. Appl. Phys. **103**, 094902 (2008).

[18] G.J. Pert, J. Comput. Phys. **49**, 1-43 (1983).

[19] G.J. Pert, J. Plasma Phys. **41**, 263-280 (1989).

[20] M.S. Qaisar and G.J. Pert, J. Appl. Phys. **94**, 1468-1477 (2003).

[21] R.K. Singh and J. Narayan, Phys. Rev. B **41**, 8843-8859 (1990)

[22] S.I. Anisimov, D. Bauerle and B.S. Luk'yanchuk, Phys. Rev. B **48**, 12076-12081 (1993).

[23] M.W. Stapleton, A.P. McKiernan and J.-P. Mosnier, J. Appl. Phys. **97**, 064904 (2005).

[24] A. Delserieys, F.Y. Khattak, C.L.S. Lewis and D. Riley, J. Appl. Phys. **106**, 083304 (2009).

[25] J. Rakovsky, P. Cermak, O. Musset and P. Veis, Spectrochim. Acta B **101**, 269-287 (2014).

[26] V. Sizyuk, A. Hassanein, V. Morozov, V. Tolkach, T. Sizyuk and B. Rice, Numer. Heat. Trans. A **49**, 215-236 (2006).

[27] J. Hoffman, T. Moscicki and Z. Szymanski, Appl. Phys. A – Mater. **104**, 815-819 (2011).

[28] T. Moscicki, J. Hoffman and J. Chrzanowska, Phys. Plasmas **22**, 103303 (2015).

[29] R.G. Watt, J. Duke, C.J. Fontes and D.D. Meyerhofer, Phy. Rev. Lett. **81**, 4644-4647 (1998).

[30] S. Rajendiran, A.K. Rossall, A. Gibson and E. Wagenaars, Surf. Coat. Tech. **260**, 417-423 (2014).

[31] A.K. Rossall, V. Aslanyan, G.J. Tallents, I. Kuznetsov, J.J. Rocca and C.S. Menoni, Laser Phys. Rev. Appl. **3**, 064013 (2015).

[32] S.L. Thompson and H.S. Lauson, Improvements in the CHART D radiation-hydrodynamic code III: revised analytic equations of state, Sandia Labs., Albuquerque, N. Mex. (U.S.A.) SC-RR-71-0714 (1974).

[33] L. Spitzer and R. Harm, Phys. Rev. **89**, 977-981 (1953).

[34] J.P. Boris and D.L. Book. J. Comp. Phys., **20**, 397-431 (1976).

[35] D.S. Kershaw, J. Comp. Phys. **26**, 43-65 (1978).

[36] J.R. Chelikowsky and M.L. Cohen, Phys. Rev. B **14**, 556-582 (1976).

[37] M.A. Green, Sol. Energ. Mat. Sol. C **92**,1305-1310 (2008).

[38] I.A.B. Zel′dovich and I.U.P. Raĭzer, Physics of shock waves and high-temperature hydrodynamic phenomena, Dover Publications (2002).

[39] T. Fujimoto and R.W.P. McWhirter, Phys. Rev. A **42**, 6588-6601 (1990).

[40] G. Cristoforetti, E. Tognoni and L.A. Gizzi, Spectrochim. Acta B **90**, 1-22 (2013).

[41] G. Cristoforetti, A. DeGiacomo, M. Dell'Aglio, S. Legnaioli, E. Tognoni, V. Paileschi and N. Omenetto, Spectrochim. Acta B **65**, 86-95 (2010).

[42] P.T. Rumsby and J.W.M. Paul, Plasma Phys. Cont. F **16**, 247-260 (1974).

[43] O. Morris, A. O'Connor, E. Sokell and P. Dunne, Plasma Sources Sci. Technol. **19**, 025007 (2010).

[44] T.L. Gilton, J.P. Cowin, G.D. Kubiak and A.V. Hamza, J. Appl. Phys. **68**, 4802-4810 (1990).

[45] A.J. Peurrung, J.P. Cowin, G. Teeter, S.E. Barlow and T.M. Orlando, J. Appl. Phys. **78**, 481-488 (1995).

[46] K.R. Chen, T.C. King, J.H. Hes, J.N. Leboeuf, D.B. Geohegan, R.F. Wood, A.A. Puretzky and J.M. Donato, Phys. Rev. B **60**, 8373-8382 (1999).

[47] J. Hoffman, T. Moscicki and Z. Szymanski, J. Phys. D: Appl. Phys. **45**, 025201 (2011).

[48] T. Nedelea and H.M. Urbassek, Phys. Rev. E **69**, 056408 (2004).

[49] A. Kramida, Yu. Ralchenko, J. Reader and NIST ASD Team (2018). *NIST Atomic Spectra Database* (version 5.5.6), [Online]. Available: https://physics.nist.gov/asd [Fri Jul 13 2018]. National Institute of Standards and Technology, Gaithersburg, MD.

[50] F. Claeyssens, R.J. Lade, K.N. Rosser and M.N.R. Ashfold, J. Appl. Phys. **89**, 697-708 (2001).

[51] F. Claeyssens, A. Cheesman, S.J. Henley and M.N.R. Ashfold, J. Appl. Phys. **92**, 6886-6894 (2002).